International Journal of Impact Engineering 187 (2024) 104926



Contents lists available at ScienceDirect

International Journal of Impact Engineering

journal homepage: www.elsevier.com/locate/ijimpeng





Numerical investigation of hypervelocity impact simulation with FEM/SPH formulation for space structures

Samet Ceri *, Zahra Sharif Khodaei

Department of Aeronautics, Imperial College London, London, SW7 2AZ, United Kingdom

ARTICLE INFO

Keywords:
Hypervelocity impact
FEM/SPH adaptive
Numerical method
Debris cloud

ABSTRACT

This paper investigates the response of aluminum structures to hypervelocity impact (HVI) and the formation of debris clouds using the Adaptive Finite Element (FEM)/Smoothed Particle Hydrodynamics (SPH) method. The main objective is to accurately replicate the response of curved thin plates to various HVIs and to characterize the resulting debris cloud shapes., for representative of shielding structures against Micrometeoroids and Orbital Debris (MMOD). In particular, the effects of different solid element formulations on the adaptive method are investigated. Experimental data from the literature is used to validate the proposed model, which is then applied to a curved thin plate subjected to varying impact angles. The findings highlight the significant influence of solid element formulation on the effectiveness of the adaptive method. Moreover, a direct correlation is observed between the impact angle and the produced debris cloud shape. These results contribute to the current knowledge on HVI responses and provide valuable insights for predicting and analyzing debris cloud formation in relation to aluminum structures.

1. Introduction

The mass and number of objects in space have sharply increased over the years due to recent advancements in space technology. This, in turn, increases the collision probability between space debris and active spacecraft. Within Earth's orbit and outer space, space debris primarily comprises natural meteoroids and artificial orbital debris, emerging as the two predominant categories [1–3]. The relative impact velocity of Meteoroid and Orbital Debris (M/OD) on in-orbit spacecraft, reaching several kilometers per second, poses an imminent danger. This kinetic energy can induce system failures or even spacecraft disintegration, potentially resulting in heavy casualties and mission failures [4,5]. While larger debris events can be mitigated through spacecraft attitude adjustments and early warning systems, the predominant challenge lies in addressing hypervelocity impacts from smaller debris, specifically Micro-Meteoroid and Orbital Debris (MMOD) of varying sizes from millimeter to microscale [2,6]. The significant abundance of MMOD particles emphasizes the need for passive protective technologies to ensure the safety of in-orbit spacecraft exposed to the evolving space debris environment [7]. This necessity becomes more pronounced, particularly considering the incapability of conventional ground-based radar systems to detect and track smaller debris objects with diameters less than 5 cm, highlighting the essential need for additional protection against MMOD impacts [8]. Therefore, it is imperative to implement additional protection to eliminate the risk posed by smaller objects [9].

The Whipple shield is a commonly employed solution for mitigating the impacts of hypervelocity space debris. The primary concept of the Whipple structure involves the placement of a shield sheet, known as a bumper, at a small distance from the main wall of the spacecraft component [10]. When debris collides with the bumper, it generates excessive shock pressures that fragment the projectile into smaller pieces, effectively dissipating and distributing the kinetic energy of the impact among these tiny debris fragments [11]. Expanding debris cloud is formed with the movement of the small debris fragments. Subsequently, tiny fragments with reduced impact energy will impinge upon the main space structure. The use of the Whipple structure significantly alleviates the potential hazardous consequences of hypervelocity impact (HVI) on the main structure. However, the impact of the debris cloud may still pose a threat by causing pitting damage over a large area on subsequent sections of the structure. Predicting the characteristics of the debris cloud may reduce the potential risk of catastrophic events caused by HVI, and can also provide valuable insight into the optimal design of the shields in order to avoid damage to the structure. Therefore, studying the debris cloud characteristics induced by HVI is vital for ensuring the operational safety of spacecraft.

Conducting experiments is the ideal approach to define the characteristics of debris clouds. However, it is both expensive and time-consuming for facilities that are able to conduct impacts at hypervelocity range. In addition, its effectiveness relies on the capabilities of

* Corresponding author.
E-mail address: samet.ceri18@imperial.ac.uk (S. Ceri).

https://doi.org/10.1016/j.ijimpeng.2024.104926
Received 12 December 2023; Received in revised form 11 February 2024; Accepted 20 February 2024
Available online 21 February 2024
0734-743X/© 2024 The Authors. Published by Elsevier Ltd. This is an open access article under the CC BY license (http://creativecommons.org/licenses/by/4.0/).

the launching and diagnostic systems [12]. Therefore, it is crucial to have robust and reliable numerical tools to comprehend the features of hypervelocity impact-induced phenomena. The Finite Element Method (FEM) is a commonly used approach for efficiently solving various engineering problems [13]. However, the mesh-based nature of this method poses challenges when dealing with hypervelocity impact problems that involve significant distortion of elements. Due to the disadvantages associated with FEM, researchers have focused on meshless methods to solve simulations that involve large deformations [14].

Meshless methods serve as the primary algorithm for simulating debris cloud formations, employing a set of independent particles to represent the structure. Due to the absence of a mesh, these algorithms can effectively address problems involving excessive deformation without the need for particle deletion. This characteristic ensures the preservation of mass, momentum, and energy within the system. Among the meshless methods, Smoothed Particle Hydrodynamics (SPH) stands out as one of the favorable approaches for addressing hypervelocity impact (HVI) problems [12]. SPH, a Lagrangian meshless method, discretizes the domain and incorporates material properties into particles [15]. Particle interactions are controlled using a kernel function [16].

However, SPH has several challenges, including tensile instability and particle inconsistency [17,18]. Tensile instability refers to the tendency of particles to cluster locally, resulting in unrealistic material fracture. This issue arises from the Eulerian characteristic of the SPH method, where the support domain of the particle of interest has defined boundaries. Neighboring particles are updated in each calculation step, allowing them to move in and out of this boundary. Consequently, the SPH method exhibits Eulerian characteristics, leading to tensile instability. To address this, the Total Lagrangian SPH formulation calculates the kernel function based on the initial configuration of the particles. By ensuring that a particle interacts with the same neighboring particles throughout the analysis, the issue of tensile instability is resolved. However, this method struggles to handle large deflections, making it unsuitable for simulating debris cloud problems [19,20].

Particle inconsistency arises due to the homogeneous distribution of particles, which reduces the accuracy of the SPH method [21]. Truncation of the kernel function by material boundaries and the presence of an inhomogeneous particle distribution contribute to this loss of consistency. To mitigate this, a kernel correction technique known as renormalization has been introduced, aiming to improve the accuracy of irregular particle spacing by imposing zeroth and first-order consistency [19,22].

SPH method is a promising method to solve HVI simulations, however, it comes with a considerable computational cost compared to the classical FEM method [13]. To enhance computational efficiency while maintaining the ability to handle large deformation problems, a reasonable solution is to combine FEM elements and SPH particles [12,23]. The use of adaptive FEM and SPH methods appears to be a practical approach that harnesses the advantages of both techniques. Preliminary studies have shown that the FEM/SPH adaptive method is a promising alternative for simulating debris cloud impact [24,25]. Zhang et al. [13] presented a coupling algorithm integrating SPH and the Finite Element Method (FEM) within a Lagrangian framework to simulate the impact of an Arne tool steel projectile on a Weldox 460 E steel target. This coupling algorithm involves the incorporation of Finite Element (FE) nodes into the SPH neighbor list to facilitate attachment, ensuring interface continuity. The interaction between SPH particles and FE nodes follows a particle-to-particle approach. Their method exhibits strong agreement with experimental ballistic limit velocity results, with a deviation of only 2%. He et al. [12] formulated an adaptive FE-SPH method and optimized the coupling method implementation for simulating debris clouds. They conducted comparisons among different implementation types and validated their results against Piekutowski's experimental study [26]. Their study reveals that the implementation type involving particle activation and coupling after element failure shows the best results, characterized by smooth particle distribution and no penetration between elements and particles. Zhang et al. [27] implemented the FEM/SPH method for hypervelocity impact simulations and compared results with Smooth Particle Galerkin (SPG), node separation, and pure SPH models. Their study demonstrated that the FEM-SPH adaptive coupling algorithm is better suited for modeling the hypervelocity impact of large-scale complex structures. However, these investigations have predominantly focused on the coupling algorithm and method implementation, while the influence of mesh behavior in FE elements remains incompletely explored.

In this study, both the solid element formulation and the mesh size effect on the accuracy of the FEM/SPH adaptive method are investigated. In addition, the effect of solid formulation on the adaptive FEM/SPH analysis is also studied as there are various formulations available and an in depth investigation is not currently available.

The comprehensive investigation of debris cloud resulting from orbital debris particle impacts becomes crucial due to the predominant occurrence of in-orbit debris impacts at oblique angles [28]. A variety of analytical models have been established to predict the behavior of normal impact loading on thin plates. In contrast, the number of developed models for oblique impacts remains relatively limited in comparison [29]. Available studies have suggested that the response of the structures to an oblique impact is significantly different from that of a normal impact [10,30–32]. Verma and Dhote [10] proposed non-dimensional empirical equations for estimating the primary fragment characteristics of a debris cloud impacting a thin flat steel plate subjected to a spherical stainless steel projectile. The impact velocities considered ranged from 2 to 4 km/s, and the angles ranged from 0° to 60°. To validate the proposed equations, a series of simulations were conducted using the SPH technique, and the results were compared with experimental data. The constants and radicals of the proposed equations were determined based on the simulation data. The predictions obtained using the proposed equations exhibited a high level of agreement with the simulation results. However this study is limited on a flat plat instead of curved structures.

In this research, the effect of solid element properties on the FEM/SPH adaptive method, specifically concerning mesh size and element formulation, is investigated in depth for the first time within the HVI regime to obtain a reliable adaptive methodology. The commercial code LS-Dyna is used as the numerical modeling platform in this research. The initial projectile velocity is set at 6.5 km/s. Numerical models are validated against experimental results published by Piekutowski, focusing on velocities at different locations within the debris cloud. [33]. Once the model is validated with a flat plate experiment, it is applied to a curved plate to understand the characteristics of debris cloud formation with different impact angles, which is more representative of real space structures. The main objective of this paper is to develop a validated methodology for debris cloud formation based on variable HVI projectiles impacting the metal Whipple shield structure, and subsequently in a follow up research to study the effect of debris cloud interaction with the main structural part which can be made of composite material.

2. Adaptive finite element-smoothed particle hydrodynamics method

The Adaptive FEM/SPH Method is a hybrid approach that addresses the limitations of traditional FEM and SPH methods in the context of HVI problems. FEM struggles with mesh-related issues and the deletion of failed elements can lead to significant mass and energy loss during calculations. On the other hand, while SPH is well-suited for debris cloud simulations, it suffers from tensile instability, inconsistencies, and high computational costs.

By combining the strengths of both methods, the FEM/SPH hybrid approach offers an efficient and robust numerical alternative for debris cloud simulations. It leverages the advantages of SPH in handling large deformation problems without being constrained by mesh limitations.

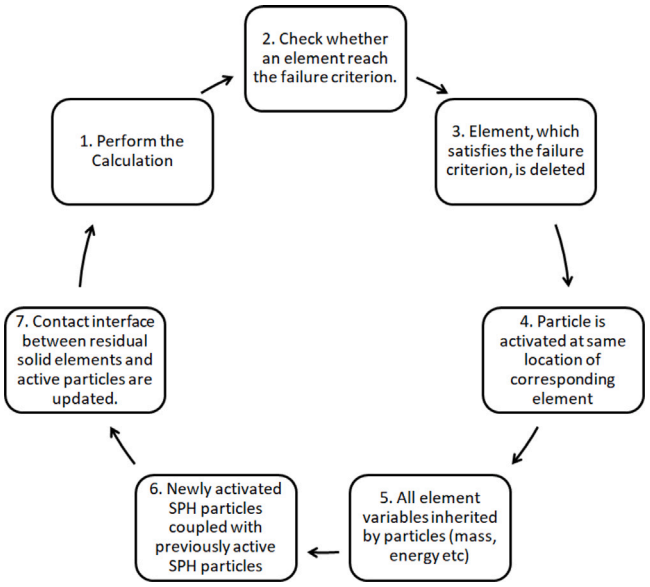


Fig. 1. Solution Process of FEM/SPH adaptive method.

The adaptive nature of the method allows elements to be converted into particles when they undergo significant deflections, ensuring accurate representation of the physical behavior. This hybrid approach overcomes the drawbacks of individual methods, making it a promising choice for simulating debris cloud phenomena in a more efficient and reliable manner.

In this approach, FE elements incapable of handling large deformations are transformed into SPH particles under significant distortions. As a result, an adequate number of less efficient but accurate particles are generated, while the remaining structure domain is represented by FE elements [24,25]. The newly generated SPH particles inherit the properties of the eroded elements, ensuring the conservation of mass, momentum, and energy in the simulation [12]. Johnson et al. [34] presented an algorithm for converting distorted elements into particles when these elements meet the failure criteria threshold. This algorithm also provides contact between residual elements and the newly generated particles. He Guang et al. [12] utilized the FEM/SPH adaptive method to simulate the debris cloud resulting from HVI. They investigated the coupling and adaptivity parameters based on the distribution of fragments within the debris cloud. Johnson et al. [35] demonstrated that the computational time of the adaptive method is lower than that of a pure SPH model. Yu et al. [36] conducted the FEM/SPH adaptive method to simulate the debris cloud generated by the impact of Zr58Nb3Cu12Ni12Al15 metallic glass on a shield plate, which caused significant damage to the witness plate. The study revealed that the FEM/SPH method can effectively simulate the distribution of the debris cloud.

Johnson and Stryk [26] proposed the Generalized Particle Algorithm (GPA) as a solution for the element conversion process in numerical simulations. The GPA utilizes the concept of equivalent plastic strain as a threshold criterion for element erosion. When the deflection degree of an element reaches the specified threshold, the element is deleted and replaced with corresponding particles. This approach ensures that the elements experiencing significant deflections are accurately represented by particles, allowing for more efficient simulations.

The processing flowchart of the FEM/SPH adaptive method is presented in Fig. 1. It illustrates the sequential steps involved in the deletion and conversion of failed elements, which in turn updates the contact interface between particles and the remaining elements. Fig. 4 provides a schematic view of the element erosion and particle activation process. In the figure, inactive particles are depicted in gray and move along with their corresponding elements, while newly activated particles are shown in green. The colored lines represent the updated contact interface between active SPH particles and the remaining elements. The activated particles are coupled with the residual elements, as demonstrated in Fig. 5. This figure demonstrates the interaction of SPH particles located near the contact interface with the standard solid elements.

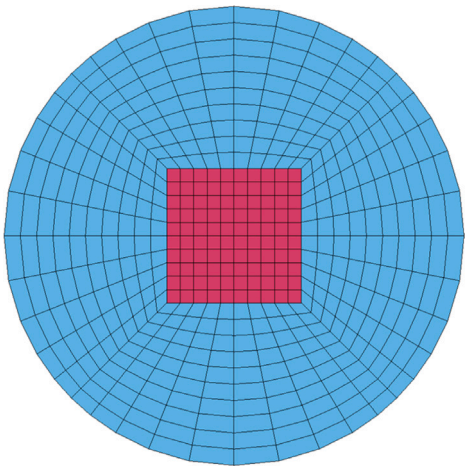


Fig. 2. Sphere Meshing with Hexahedral Elements.

2.1. Finite element modeling

There have been various configurations of solid elements introduced over the years. The most widely used grid shapes in FEM are tetrahedral or hexahedral elements [37]. Hexahedral elements are generally preferred over tetrahedral elements in structural engineering problems due to their higher accuracy and efficiency [37,38]. However, it is challenging to mesh a sphere-based domain with identical mesh size using hexahedral elements. Commercial software such as Ls-Dyna employs default mesh generation algorithms for sphere structures with varying element size distribution. The mesh distribution of a sphere is illustrated in Fig. 2. As shown in the figure, meshing a sphere using hexahedral elements can be divided into two areas: the cubic center and the transition region. The center of the sphere is modeled using identical cubs, highlighted in red. Conversely, the size of the mesh varies in the transition region, depicted in blue. This inhomogeneity may lead to inconsistencies when solid elements are converted into SPH particles. Refining the mesh in the sphere can alleviate these inconsistencies by reducing the differences in element size.

Over the years, various hexahedral solid element formulations have been proposed, focusing on integration points and aspect ratios. Each formulation exhibits distinct advantages and disadvantages. The widely used 8-node brick hexahedron element, employing a single integration point at the element centroid, is known for its computational efficiency and robustness in large deformations compared to other formulations [39]. However, the main issue with this element formulation is the requirement of hourglass treatment [40]. Another formulation, known as the fully integrated element, utilizes eight integration points (ELFORM=2) [41]. Schematic representations of these element formulations are presented in Fig. 3. The fully integrated formulation resembles the classical method in terms of calculation but eliminates the need for hourglass treatment due to its increased number of integration points. Nevertheless, it is recognized that elements employing multiple integration points are more susceptible to large distortions, leading to shear locking issues. Shear locking manifests as stiffness in

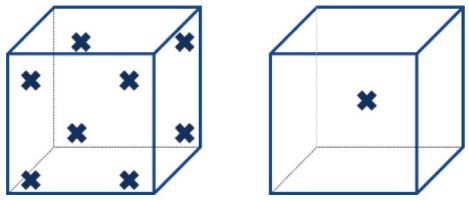


Fig. 3. Integration Point Illustration of Solid Element Formulation.

elements, particularly when the aspect ratio is poor [42]. To overcome shear locking issues, two new element formulations were introduced, which employ an assumed strain approach for elements with poor aspect ratios. These formulations are known as the accurate formulation fully integrated elements with poor aspect ratios (ELFORM=−2) and the efficient formulation fully integrated elements with poor aspect ratios (ELFORM=−1). The efficient formulation reduces the gradient-displacement matrix compared to the accurate formulation, resulting in reduced computational cost [43]. However, no investigation has been reported on the compatibility of the different FE element formulation with SPH particles, and this is one of the main objectives of this paper.

2.2. SPH modeling

SPH particles interact with the neighbor particles through a smoothing function within their support domain. In the FEM/SPH coupling method, the particles near the contact interface consider the FE nodes, located inside the support domain, as their neighboring particles. This allows the smoothing function to extend beyond the boundary, thereby avoiding any boundary effects or inconsistencies. The contact principle between SPH and FEM is achieved through the summation extension of SPH with the nodes of the FE elements located within the support domain. The specific approximation methods employed depend on the particle's position and the type of discretization. For particles located far from the interface, a pure SPH approximation is utilized. On the other hand, for SPH particles near the boundary interface, the FE nodes within the support domain are included in the SPH summation. Furthermore, the FE elements are approximated using the pure FEM approximation formulation. The overall approximation formulation, considering both position and discretization mode, can be expressed as follows [13]:

SPH only:

$$\langle \nabla f(x_i) \rangle = \sum_{j=1}^{N} \frac{m_j}{\rho_j} f(x_j) A_{ij} \tag{1}$$

FEM/SPH coupling:

$$\langle \nabla f(x_i) \rangle = \sum_{j=1}^{N} \frac{m_j}{\rho_j} f(x_j) A_{ij} + \sum_{j=1}^{N_b} \frac{m_{bj}}{\rho_{bj}} f(x_j) A_{ij} \tag{2}$$

FEM only

$$\langle \nabla f(x_i) \rangle = \sum_{i} N_i(x) f(x_i) \tag{3}$$

3. Debris cloud model

The Whipple structure, comprising of a front plate (referred to as the bumper or shield) and a rear plate (known as the witness plate or main wall), offers excellent protection against the impact of space debris on spacecraft. Upon impact, the projectile and the shield plate break into smaller fragments, forming a debris cloud in response to the generated shock wave. The debris cloud consists of fragments with lower energy than the initial kinetic energy of the projectile. As the debris cloud expands, the energy is distributed more widely, reducing the severity of damage to the rear wall [44]. However, the debris cloud still poses

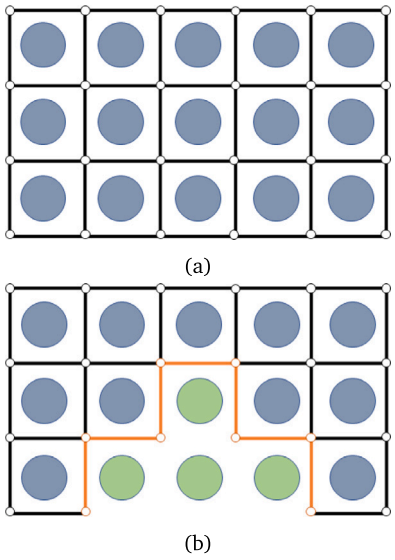


Fig. 4. FEM/SPH adaptive mesh (a) before element conversion (with passive SPH particles), (b) Activated Particles with updated boundary.

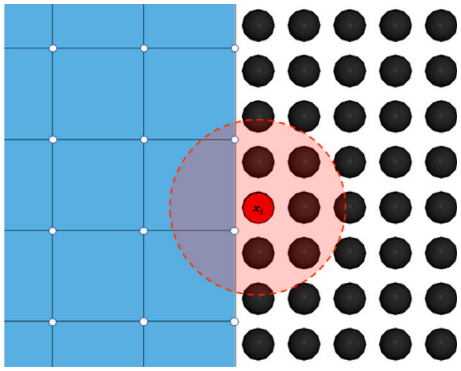


Fig. 5. Coupling of SPH particles and FE elements at the contact interface.

a significant threat to the structural integrity of the rear wall. Hence, it is crucial to investigate the impact of HVI-induced debris clouds to ensure the safety of spacecraft missions.

Piekutowski [26] conducted a series of HVI impact experiments on an aluminum Whipple structure using a two-stage light gas gun. The experiments involved varying velocities and dimensions of the projectiles. Flash X-rays were employed to visualize and record the positions of both the projectile and the debris cloud, allowing for the determination of velocities at different locations within the debris cloud. The X-ray views, as shown in Fig. 6, demonstrates the impact of a 9.53 mm diameter sphere made of 2017-T4 aluminum alloy with a velocity of 6.62 km/s on a 0.46 mm thick 6061-T6 aluminum plate. According to Piekutowski, the debris cloud can be divided into three major components: the ejecta veil, the external bubble, and the internal structure. The ejecta veil is primarily composed of fragments from the bumper and is ejected as a result of the impact. The external bubble of debris is formed around the sides of the debris cloud and mainly consists of bumper fragments. The internal structure, on the other hand, is composed of shattered projectile elements and is divided into front, center, and rear components.

Piekutowski characterized the debris cloud based on its velocities, which were measured using radiographs. Ten measurement points at various locations within the debris cloud, as shown in Fig. 7, were defined for velocity measurements [26]. The axial and radial velocities of the debris cloud were determined using the positions of these

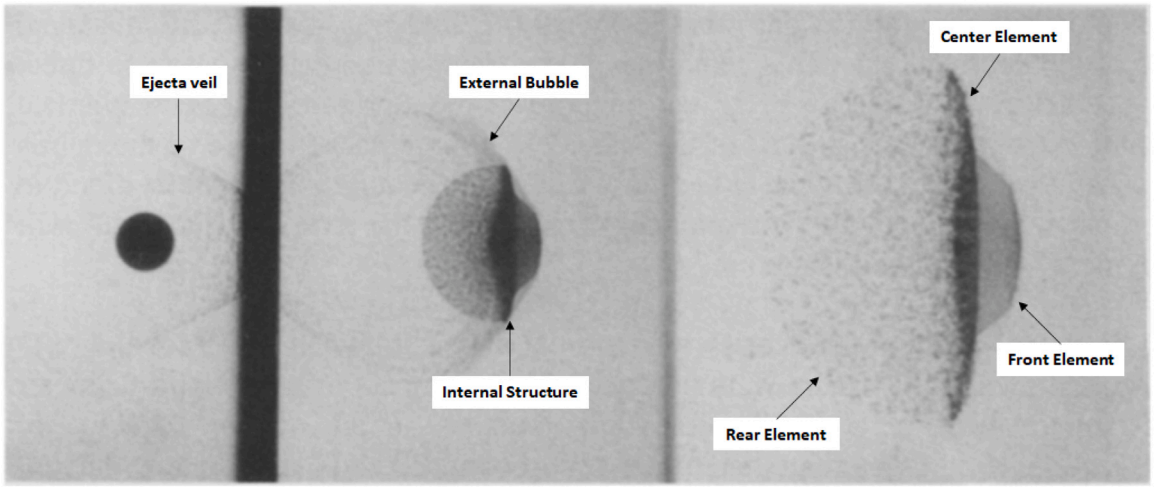


Fig. 6. Views of debris clouds produced by impact of 9.53 mm diameter aluminum spheres on aluminum plate [26].

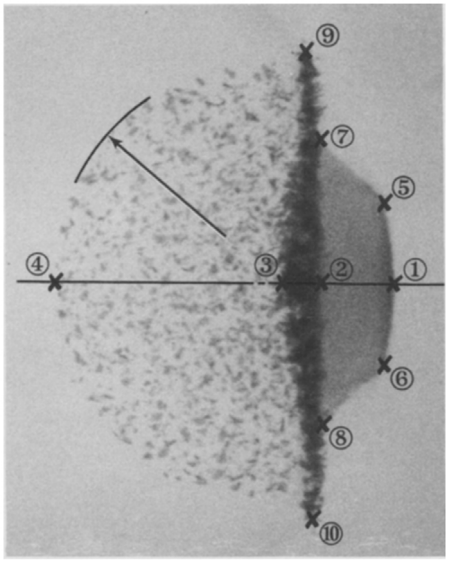


Fig. 7. Velocity measurements of the debris cloud using designated points [26].

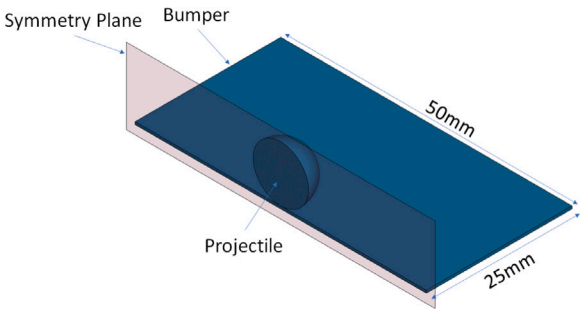


Fig. 8. Schematic view of the numerical model.

measurement points in the radiographs. The normalized velocity data was obtained by dividing the measured velocity by the impact velocity of the projectile. However, most of the tests were performed with direct impact of aluminum spheres on a flat bumper plate. In the present research, the effect of the solid element formulation on the adaptive FEM/SPH formulation is investigated by comparing the numerically obtained velocities with the experimental data. The validated model was then used to investigate the impact with oblique angles on curved plates.

4. Numerical method: A parametric investigation for modeling HVI

In order to investigate the effect of FE element properties on adaptivity under the HVI regime, FEM/SPH adaptive models were developed considering different mesh densities and element formulations. The commercial software LS-Dyna was utilized to simulate the HVI scenarios. Adaptive FEM-SPH meshes were constructed to represent the structures, and the results were compared against experimental data obtained by Piekutowski [26]. Both the plate and the projectile are modeled using adaptive FEM/SPH meshes in all numerical models. Mesh size of the plate and projectiles are shown in the 2. The reference data corresponded to the impact of a 9.53 mm sphere made of 2017-T4 aluminum alloy on a 6061-T6 aluminum plate, with an impact velocity of 6.62 km/s and a bumper thickness to projectile diameter ratio (t/D) of 0.049. The schematic view of the numerical models is presented in Fig. 8. Hexahedral grid shapes were employed for the FE meshes. The shield plate, also known as the bumper, had dimensions of 50 mm × 50 mm × 0.47 mm. All edge surfaces of the bumper were constrained in all directions. All edge surfaces of the bumper were constrained in all directions. Due to the presence of a symmetry plane, only half of the structure was modeled. The eroding contact algorithm with the soft constraint formulation was applied between the solid elements of the projectile and the plate. The projectile was considered as the slave segment, while the plate elements served as the master segments. Friction effects were neglected.

In the numerical models, it was crucial to select an element size that balanced precision in capturing the material response with minimal computational time. The findings from a preliminary mesh sensitivity study revealed that optimal convergence occurred with an element size of approximately 0.1 mm for the plate.

In this study, the properties of aluminum were modeled using the Johnson-Cook material model and the Mie-Gruneisen Equation-of-State (EOS) [12,45]. The material parameters of 2024-T3 aluminum were adopted for the projectile, as this material was readily available and exhibited similar performance to the aluminum used in the experimental data [27,46]. The maximum tensile stress was chosen as the failure criterion for both materials. The material properties are summarized in Table 1. The Johnson-Cook (J-C) material model is widely used to describe high-velocity impact deformations in metallic structures [36]. However, the J-C model does not capture the spall phenomenon that

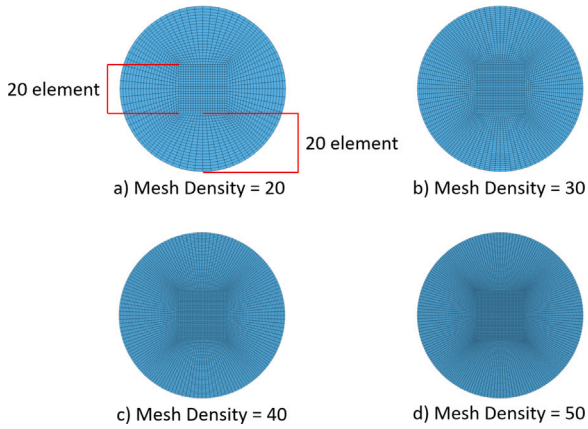


Fig. 9. Spherical Projectile with different mesh density.

occurs when the condition of tensile shock waves exceeding the material's endurance is reached. Therefore, a fracture model based on the maximum principal stress was defined in the simulation to simulate the spall phenomenon [47]. In this fracture model, if the maximum principal stress σ_max, exceeds the tensile stress σ_p, the tensile stress is reset to zero. The same material parameters were assigned to the solid FE elements and the corresponding newly generated SPH particles. The effect of temperature was neglected in this study. SPH formulation was employed for the particles in the simulation. The ratio of the smoothing length to the particle spacing (CSLH) was set to 1.5 [48]. Monaghan's artificial viscosity was incorporated into the SPH calculation to prevent non-physical oscillations of the particles induced by shock waves [49].

In the Johnson-Cook material model, yield stress σ_y is calculated as [50]:

$$\sigma_y = \left(A + B\epsilon_p^n\right)\left(1 + C ln\frac{\dot{\epsilon}_p}{\dot{\epsilon}_n}\right)\left(1 - (T^*)^m\right) \tag{4}$$

where σ_y is the yield stress, ϵ_p is the equivalent plastic strain, $\dot{\epsilon}_p$ is the plastic strain rate, $\dot{\epsilon}_0$ is the reference strain rate. A is the yield strength of the material, B is the hardening constant and n is the hardening exponent, C is the strain rate coefficient, $T*$ is the relative temperature $(T *= (T - T_r)/(T_m - T_r))$ where T_r is the room temperature and T_m is the melting temperature, and m is the thermal softening index.

Also, the Mie-Grüneisen equation of state (E.O.S.) defines the pressure as follows [27]:

For compressed materials:

$$p = \frac{\rho_0 C^2 \mu\left[1 + (1 - \frac{\gamma_0}{2})\mu - \frac{a}{2}\mu^2\right]}{\left[1 - (S_1 - 1)\mu - S_2\frac{\mu^2}{\mu+1} - S_3\frac{\mu^3}{(\mu+1)^2}\right]^2} + (\gamma_0 + a\mu)E \tag{5}$$

And for expanded materials:

$$p = \rho_0 C^2 \mu + (\gamma_0 + a\mu)E \tag{6}$$

Here, γ_0 represents the Gruneisen coefficient, ρ_0 is the initial density of the material, and C represents the sound velocity through the material. Additionally, E denotes the Young Modulus, while S_1, S_2, and S_3 are the Hugoniot slope coefficients. Moreover, μ represents the nominal strain, calculated as $\mu = 1 - \rho_0/\rho$.

The homogeneous mesh distribution is crucial for obtaining accurate results with hexahedral elements. Therefore, the mesh size of the plate was set to 0.1 mm, and 5 elements were used through the thickness of the plate. The mesh size of the projectile was one of the parameters investigated in this study. LS-Dyna software provides a meshing algorithm that discretizes the spherical structure using hexahedral elements. In this algorithm, the center of the sphere is meshed using an identical grid size, while the remaining portion of the sphere is

Table 1
Material parameters of the projectile and the shield [12].

Parameter	Unit	Al 2024-T3	Al 6061-T6
Mie-Gruneisen Equation of State			
Density	g/cm^3	2.77	2.77
Gruneisen coefficient	–	1.97	1.97
Parameter C_0	km/s	5.386	5.386
Parameter S_1	–	1.339	1.339
Johnson-Cook Strength Model			
Shear modulus	GPa	27.6	27.6
Yield Stress	MPa	265	290
Hardening constant	MPa	426	203
Hardening exponent	–	0.34	0.35
Strain rate coefficient	–	0.015	0.011
Effective plastic strain rate	1/s	1	1
Failure parameters D_1	–	0.8	1
Failure parameters D_{2-5}	–	0	0
Failure Model			
Maximum tensile stress	GPa	2.6	2.6

Table 2
Number of elements and element sizes for models with varying mesh densities.

Mesh density	Number of element	The size of the longest element
20	28 000	0.473 mm
30	94 500	0.316 mm
40	224 000	0.237 mm
50	437 500	0.189 mm
Plate	625 000	0.1 mm

modeled using elements of varying sizes, as shown in Fig. 2. This region where the element size varies is referred to as the transition area of the sphere.

To examine the impact of mesh size on the FEM/SPH adaptive method, four different projectiles were modeled, each with different mesh size. Their computational costs were compared to assess the efficiency of the mesh sensitivity. Furthermore, the accuracy and efficiency of different solid element formulations were also compared.

An equal number of elements is used in both the center and the transition region. The distribution of elements is depicted in Fig. 9(a). Four different spherical mesh densities were compared: Mesh density-20, Mesh density-30, Mesh density-40, and Mesh density-50. The number of elements and the size of the longest element associated with each mesh size are presented in Table 2.

The mesh density of the spherical projectile can influence the results of adaptivity due to the uneven element size distribution through the transition region caused by the spherical meshing approach. Increasing the mesh density leads to smaller element sizes, resulting in reduced particle spacing when an element fails and is converted into a particle. This reduction in particle spacing can help mitigate instabilities and inconsistencies.

The results of the study revealed that the mesh density of the spherical adaptive solid elements has a significant impact on the shape of the debris cloud. Higher mesh densities demonstrated better agreement with the experimental study.

In this study, four different solid element formulations were compared with experimental results using a mesh density of 40 for the spherical projectile. The element formulations examined were as follows:

1. Reduced Integration point (ELFORM=1): This is the default element formulation in LS-Dyna for solid elements. It has one integration point at the center of the element, which leads to faster solutions due to the reduced number of integration points. However, under large deflections, this formulation requires the application of an hourglass treatment to prevent hourglass-type

instabilities. In this study, the Flanagan-Belytschko viscous form of hourglass with exact volume integration was implemented for the ELFORM=1 model, as recommended in the literature [12,39,51]. The hourglass coefficient was set to 1 in this study, however in the referenced literature no hourglass parameter was used.

2. Fully integrated solid element (ELFORM=2): This formulation uses fully integrated elements, where integration points are distributed throughout the element. It does not require an hourglass treatment and provides more accurate results compared to the reduced integration formulation.
3. Efficient formulation fully integrated elements with poor aspect ratios (ELFORM=−1): This formulation is specifically designed for elements with poor aspect ratios. It uses fully integrated elements and aims to provide an efficient solution while maintaining accuracy.
4. Accurate formulation fully integrated elements with poor aspect ratios (ELFORM=−2): Similar to ELFORM=−1, this formulation is also designed for elements with poor aspect ratios. It employs fully integrated elements and aims to achieve even more accurate results.

The comparison of these different element formulations with experimental results was conducted to assess their accuracy and performance.

5. FEM/SPH adaptive model validation

The results are presented in two sections with regards to mesh density and element formulations. The debris cloud structures obtained from the numerical simulations at 7 μs are shown in Fig. 11, focusing on different mesh densities, and Fig. 12, for the different solid element formulations. The first row is the full view of the debris cloud, while the second row is the zoomed-in view to examine the internal structure. The third row illustrates the remaining part of the solid elements of the projectile after erosion. Green particles represent the particles generated from the plate, while brown particles represent the particles generated from the shattered projectile. The velocities in the numerical simulations are calculated by averaging the velocities of 200 particles at specific points in the debris cloud. Tables 3 and 4 compare the velocity values obtained from the numerical models with the experimental data [33] at the defined velocity measurement points.

The numerical model that exhibits the best agreement with the experiment is highlighted in green.

5.1. Mesh densities

Fig. 11 illustrates the debris cloud shape obtained by different mesh densities. The residual elements of the projectile vary with the mesh size. Increasing the mesh density results in more elements remaining unconverted into SPH particles in the center of the sphere. The mesh density variation has a significant influence on the shape of the debris cloud. Specifically, the front elements of the internal structure and the external bubble exhibit notable differences between the models with lower and higher mesh densities.

In Fig. 11(a), it can be observed that more green particles (generated from the bumper) cluster in front of the debris cloud instead of being distributed throughout the external bubble compared to the other mesh density models. The shape of the ejecta veil is also influenced by the mesh density of the projectile. Lower mesh densities yield nonphysical ejecta veil shapes due to significant particle clustering, as shown in Fig. 11(a) and (b). This clustering arises from the tensile instability issue of the SPH method. With larger particle spacing, the number of neighboring particles decreases, leading to artificial particle clustering.

In contrast, higher mesh density models exhibit more regular particle distributions, as seen in Fig. 11(c) and (d). This is because a greater number of particles can be encompassed within the support domain, allowing for increased particle interaction and reduced artificial particle clustering.

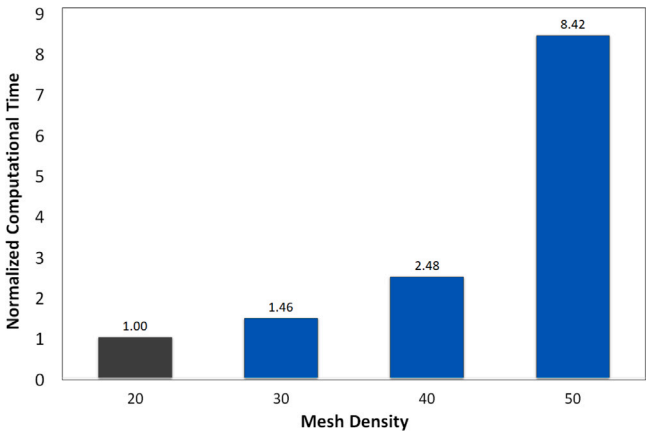


Fig. 10. Comparison of the computational time for different mesh densities (normalized with respect to Mesh Density=20).

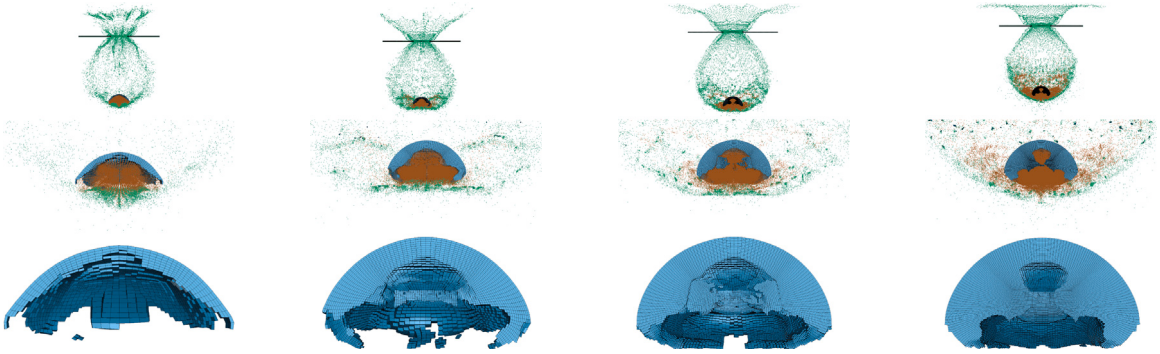
Overall, the analysis of mesh densities highlights that the debris cloud shape, distribution of particles, and behavior of the ejecta veil are influenced by the mesh density of the projectile. Higher mesh densities provide more accurate and realistic results, while lower mesh densities can introduce nonphysical artifacts such as particle clustering.

All simulations were conducted using 48 CPUs of the Intel processor. The computational comparisons of the numerical meshes are presented in Fig. 10, where CPU times are normalized with respect to the Mesh Density=20 model, which took 8 h and 8 min to complete. It can be observed that the computational cost increases as the mesh density increases due to the larger number of generated SPH particles. This is an expected outcome since the computational cost of SPH is significantly higher compared to the classical FEM method [35]. Specifically, the computational cost of the Mesh Density=50 model is 8.42 times higher than that of the Mesh Density=20 model. On the other hand, the computational cost difference between the Mesh Density=40 and Mesh Density=20 models is approximately 2.5 times. Specifically, there is a considerable change in the calculation speed between the Mesh Density=40 and Mesh Density=50. These findings show the relationship between computational cost and accuracy when using varying solid mesh densities in Adaptive FEM/SPH scheme. While higher mesh densities can provide more accurate results, they result in increased computational cost.

After a short time of impact, the debris cloud shape reaches a stable state where its features do not change significantly [52]. Piekutowski [33] defined the characteristics of the debris cloud based on velocities measured at specific locations within the cloud. In the numerical simulation, the measured velocities are normalized with respect to the impact velocity, and these normalized velocities are compared against Piekutowski's experimental data [53] in Table 3.

The results demonstrate that the accuracy of the obtained velocity increases with higher mesh densities. Among the different mesh densities, Mesh Density=20 shows the largest discrepancy compared to the experimental data. Velocities at points 2 (V2) and 3 (V3) have an error of approximately 3% in comparison to the experimental value. On the other hand, Mesh Density=30 shows the best agreement with the experimental data for velocities along the axial direction at points 7 ($V7^a$) and 9 ($V9^a$). Mesh Density=50 exhibits the best convergence with the experimental data for velocities measured along the centerline of the debris cloud, which includes points 1–4. Additionally, Mesh Density=40 provides the best agreement with the experimental data for velocities measured in diagonal directions. However, the difference between the velocities of Mesh Density=40 and Mesh Density=50 is less than 1%.

Overall, it is observed that the accuracy of the results increases as the element size decreases. Smaller elements lead to a reduced particle



(a) mesh20 (b) mesh30 (c) mesh40 (d) mesh50

Fig. 11. Obtained debris cloud formation and residual projectile elements across different mesh densities.

Table 3
Comparison of normalized velocities from numerical simulations with experimental data by Piekutowski [33] across different mesh densities.

Mesh density	V1/V0	V2/V0	V3/V0	V4/V0	V5[a]/V0	V5[d]/V0	V7[a]/V0	V7[d]/V0	V9[a]/V0	V9[d]/V0
20	0.982	0.953	0.947	0.787	0.954	0.079	0.928	0.125	0.846	0.234
30	0.967	0.960	0.948	0.801	0.961	0.081	0.935	0.125	0.890	0.252
40	0.977	0.962	0.952	0.814	0.963	0.083	0.926	0.137	0.876	0.255
50	0.986	0.962	0.958	0.822	0.963	0.082	0.929	0.138	0.875	0.253
Experiment [33]	1.012	0.980	0.977	0.826	1.010	0.084	0.976	0.137	0.968	0.254

[a] axial
[d] diameter

Table 4
Comparison of normalized velocities from numerical simulations with experimental data by Piekutowski [33] across different element formulations.

Formulation	V1/V0	V2/V0	V3/V0	V4/V0	V5[a]/V0	V5[d]/V0	V7[a]/V0	V7[d]/V0	V9[a]/V0	V9[d]/V0
ELFORM=1	0.945	0.928	0.926	0.757	0.924	0.088	0.892	0.126	0.856	0.234
ELFORM=2	0.968	0.950	0.946	0.778	0.956	0.084	0.924	0.130	0.885	0.269
ELFORM=−1	0.977	0.962	0.952	0.814	0.963	0.083	0.926	0.137	0.876	0.255
ELFORM=−2	0.976	0.960	0.952	0.822	0.961	0.084	0.923	0.137	0.884	0.257
Experiment [33]	1.012	0.980	0.977	0.826	1.010	0.084	0.976	0.137	0.968	0.254

[a] axial
[d] diameter

spacing, resulting in more particles being considered as neighboring particles during particle approximation. This helps to alleviate the tensile instability issue that depends on particle distribution.

The mesh density is identified as a key parameter in the FEM/SPH adaptive method due to its influence on the particle spacing of generated SPH particles. Among the numerical models, Mesh Density=40 appears to be the best option considering both computational cost and accuracy.

5.2. Element formulation

The effect of element formulation on the FEM/SPH adaptivity for HVI-induced debris cloud is presented in this section. Fig. 12 displays the numerical results obtained using four different solid element formulations at 7 μs, based on the HVI impact simulation conducted by Piekutowski [33]. The results show that the choice of element formulation has a significant effect on the shape of the debris cloud and the erosion pattern of the projectile. Furthermore, the expansion of particles from the projectile (brown color) within the debris cloud varies with different element formulations. It is worth noting that particle clumping is observed in all simulations.

The results obtained from the numerical simulation using different solid element formulations are presented in Table 4. The velocities of the debris cloud are compared with experimental data to evaluate the accuracy of the different element formulations. Among the different formulations, the ELFORM=1 model, which uses one Node Integration Point (NIP) per element, shows the largest discrepancy with the experimental data for all velocities, with errors ranging from approximately 7% to 24%. This suggests that using a single NIP per element is not sufficient to capture the complex behavior of the debris cloud accurately. On the other hand, increasing the number of NIPs per element significantly improves the accuracy of the numerical calculations. Additionally, the modifications in the Jacobian matrix (ELFORM=−1 and ELFROM=−2)lead to better agreement with the experiment compared to the classical 8 NIP hexahedral brick element. The difference in velocities between the ELFORM=−1 and ELFORM=−2 models is less than 1%. In contrast, the computational speed of the ELFORM=−2 is around 8% slower than ELFORM=−1.

The findings indicate that increasing the number of NIPs reduce the errors in velocity prediction, leading to improved agreement with the experimental data. Importantly, the computational cost of the simulation remained comparable for all element formulation, with differences in calculation speed of less than 10%. This suggests that the enhanced accuracy achieved by employing element formulations with multiple NIPs does not significantly impact the computational efficiency. Consequently, implementing element formulations with multiple NIPs is a favorable choice as it improves simulation accuracy without incurring substantial additional computational costs.

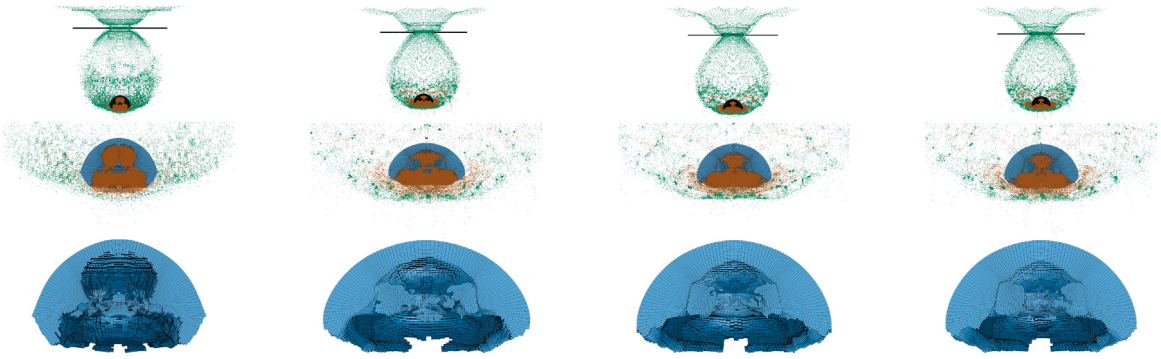


Fig. 12. Obtained debris cloud formation and residual projectile elements across different element formulations.

Overall, the numerical simulations demonstrate reasonable agreement with the experimental data, with errors ranging from approximately 1% to 3%. This suggests that the selected element formulations effectively capture the response of the curved panel under hypervelocity impact. However, certain discrepancies between the numerical and experimental velocities may arise due to uncertainties in material properties, boundary conditions, and simplifications in the numerical model.

6. Numerical modeling of curved panel impact

In this section, HVI impact on the curved aluminum panel made of 6061-T6 alloy is investigated. The panel is subjected to impacts at various angles (α), including 0°, 15°, 30°, 45°. The simulations in this section utilize the numerical model parameters that have been validated in the previous section. The curved panel has dimensions of 640 mm in width and 50 mm in length, with a radius of 50 mm and a thickness of 0.47 mm. To simulate the boundary conditions, the edges along the length of the curved panel are clamped. To reduce computational costs, only half of the structure is modeled using a symmetry plate. The velocity of the projectile used in this section remains the same as in the previous section which is 6.62 km/s. The same material properties are assigned to the curved panel as those used for the flat panel in the previous section. The numerical set-up of the curved panel models is presented in Fig. 13, where α is impact angle and V is velocity and R is the radius of the curved panel. The HVI response of the curved panel under different angles is investigated by analyzing the debris cloud shape. Fig. 14 illustrates the produced debris cloud and its characteristic parameters. The boundary of the debris cloud is indicated by the red line in the figure. The defined characteristic parameters, L1- the debris cloud length, L2- distance from the front end of the ejecta veil to the impact center, L3- length of the ejecta veil, D1-the maximum diameter of the debris cloud, D2- the maximum diameter of the ejecta veil, D3- distance from the end of the ejecta veil to the impact center. The results obtained from the simulations are summarized in Table 5 and Figs. 15–18. The Table 5 reveals the significant observations regarding the direct impact (angle of 0° impact) on both flat and curved panels. Firstly, the values of L1, L2, and D1 exhibit remarkable similarity, with differences of less than 1%. This finding suggests that the curvature of the panel does not have a significant impact on the debris cloud, ejecta length, and debris cloud diameter. In addition, it is noteworthy that the ratio of D3 to D2 remains consistently at 0.5 for both models. This indicates that both configurations maintain a symmetrical shape for the ejecta veil. On the other hand, when comparing the D2 and D3 values, there is notable discrepancy can be seen. The curved plate exhibits a larger maximum diameter of the ejecta veil (D2) of 84, surpassing the flat plate's D2 value of 72 by approximately 16.7%. Similarly, the distance from the end of the ejecta veil to the impact center (D3) is slightly

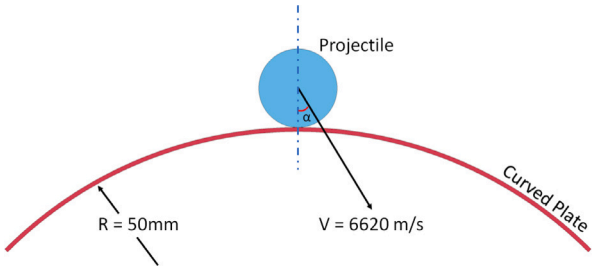


Fig. 13. Numerical Model Set-up of the Curved Panel.

Table 5
Variation in debris cloud parameters at impact on a curved plate with different impact angles.

	L1	L2	L3	D1	D2	D3
Flat Plate 0	44.2	14.5	0	40.2	72	36
Curved Plate 0	44.6	14.6	0	40.6	84	42
Curved Plate 15	43.4	16.1	8.04	38.3	104.4	81.8
Curved Plate 30	41.6	18.2	12.1	35.5	105.6	82.9
Curved Plate 45	38.4	13.7	33.6	32	85.6	82.9

greater for the curved plate (42) compared to the flat plate (36). These differences indicate that the plate curvature have significant influence on the dimensions of the ejecta veil.

Fig. 15 illustrates the length (L1) change by different impact angles. According to the figure, L1 length decreases almost linearly as the impact angle increases. At higher angles, the reduction in length is more noticeable, indicating a more localized distribution of debris.

The decrease in debris cloud length with increasing impact angle can be attributed to changes in the velocity components. As the impact angle increases, more of the velocity is directed tangentially to the surface, reducing the axial velocity component. This leads to a shorter penetration depth and a corresponding decrease in debris cloud length. This phenomenon is commonly observed in oblique impacts, where the conservation of momentum causes the axial velocity component to decrease to compensate for the increase in the tangential component. As a result, the debris cloud formed at higher impact angles has a more localized distribution and a shorter length.

The investigation of lengths L2 and L3, as well as their corresponding ratio L3/L2, is assumed to have a valuable means of understanding the characteristics of debris characteristic on curved surfaces. From the Table 5, it can be seen that both L2 and L3 show a consistent increase as the impact angle increases. This suggests a wider dispersion of debris along the surface and a larger distance covered by the debris cloud from the impact center at the rear side of the shield. However, at the impact angle of 45 degrees, the value of L2 decreases significantly to 13.7 mm. This indicates that the ejecta veil dispersion along the surface is more

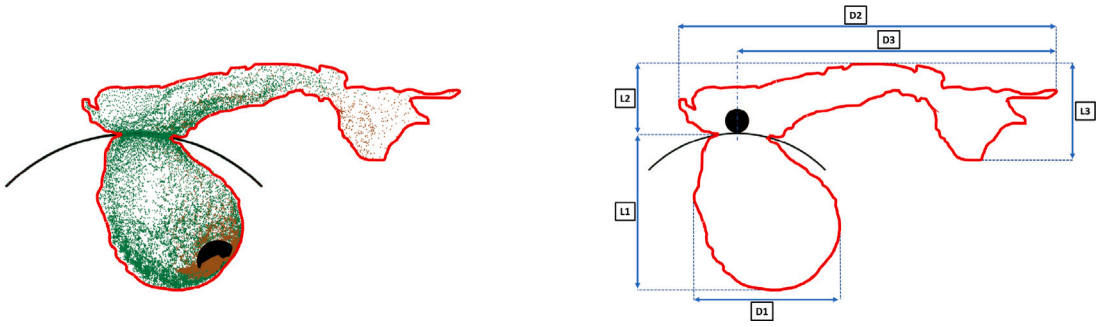


Fig. 14. Debris cloud obtained after numerical oblique impact on the curved panel and Debris Cloud Parameters.

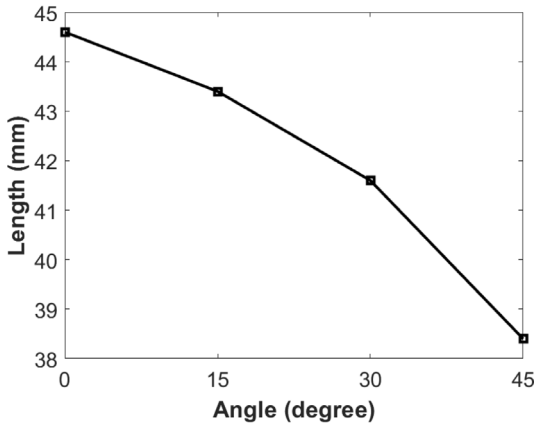


Fig. 15. L1 Changes with the impact angle.

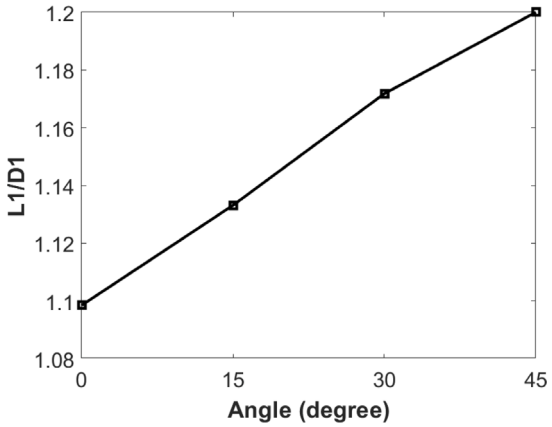


Fig. 16. L1/D1 ratio Changes with the impact angle.

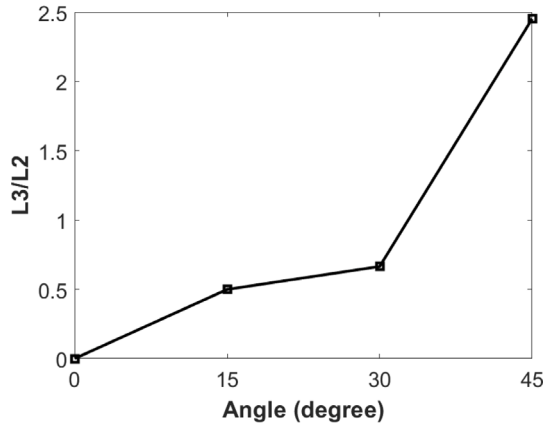


Fig. 17. L3/L2 Changes with the impact angle.

localized, with the ejecta veil traveling a shorter distance towards the rear. In addition, the ratio L3/L2, shown in Fig. 17, has an increasing trend with increasing impact angle. It is interesting to observe that at 0-degree impact angle (direct impact), L3 is measured as 0, indicating no ejecta veil length. On the other hand, however, as the impact angle increases, the distance covered by the debris cloud from the impact center expands. Specifically, at a 45-degree impact angle, L3 becomes approximately 2.5 times larger than L2, indicating a significant increase in the ejecta veil length.

The analysis of the L1/D1 ratio (see in Fig. 16) reveals important findings in this regard. At a 0° angle, the ratio is approximately 1.07, indicating a relatively equal distribution of debris along the length and diameter of the impact area. However, as the impact angle increases, the ratio gradually decreases, suggesting a more concentrated dispersal of debris. This trend becomes more pronounced at higher angles, such as 45°, where the ratio drops to around 1.20, indicating a narrower dispersion debris cloud pattern (see Fig. 16-Fig. 18).

The ejecta veil dispersion diameter ratio D3/D2 is presented in the Fig. 19. As observed in the figure, the ejecta veil disperses in the impact direction as the angle increases. The D3/D2 ratio is 0.5 at the direct impact (0-degree impact angle), as expected due to symmetrical shape of the ejecta veil, while it reaches 0.97 at 45°. However, this ratio does not change considerably between 15° and 30°, where D3 and D2 values increase at a similiar ratio.

7. Conclusion

In this paper, the FEM/SPH adaptive method is utilized to simulate HVI impact scenarios. The primary objective of this research is to investigate oblique HVI impacts on curved panels by employing the most effective numerical model. To achieve this, a parametric study was conducted to explore the influence of solid element features, including mesh density and element formulation, on the FEM/SPH adaptive method, considering the characteristics of the debris cloud. The numerical results were then compared with data from existing literature to validate the model. The validated model was subsequently employed to analyze oblique HVI impacts on the curved panel.

The following key findings have emerged from the parametric study:

1. Mesh density of the solid elements plays a crucial role in the accuracy of the FEM/SPH adaptive method. Coarser meshes result in higher particle spacing, leading to uneven particle distribution and reduced accuracy. Increasing the mesh density improves the accuracy of the simulation by decreasing the particle spacing. However, higher mesh densities significantly increase the

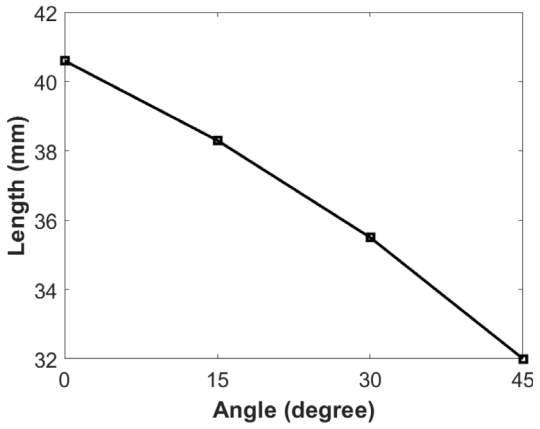


Fig. 18. D1 Changes with the impact angle.

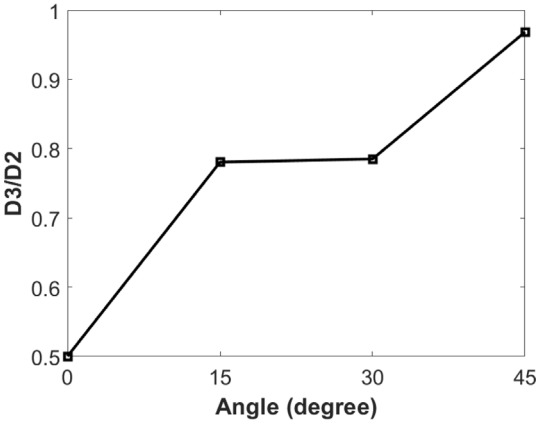


Fig. 19. D3/D2 Changes with the impact angle.

computational cost due to the generation of additional SPH particles.

2. The number of integration points of the solid element formulation has a significant impact on the debris cloud shape and the remaining part of the projectile. Increasing the number of integration points improves the accuracy of the FEM/SPH adaptive method. In particular, the use of 8-node integration points and modifications in the Jacobian matrix (efficient, accurate formulations) enhance the accuracy of the simulation compared to the 1-node integration point model.

The results obtained from the FEM/SPH adaptive method have been validated against experimental data, showing good agreement. However, it is important to note that particle clumping was observed in all simulations, indicating the presence of tensile instability issues in the SPH method.

Additionally, the influence of impact angle on the curved plate and its effect on the resulting debris cloud shape from HVI impacts was investigated. It was observed that curvature on the plate contributed to longer displacement of the ejecta in the diagonal direction, resulting in a larger ejecta veil diameter. Furthermore, as the impact angle increases, the length of the debris cloud (L1) decreases. This reduction can be attributed to a higher proportion of velocity being directed in the diagonal direction, leading to a shorter axial penetration of debris and a corresponding decrease in its length. Moreover, as the oblique angle increased, the diameter of the ejecta veils and their penetration in the diagonal direction also increased.

This study demonstrates the potential of characterizing debris cloud shapes using the FEM/SPH adaptive method. However, to enhance the accuracy of the findings presented, further analysis and experimental validation are recommended to confirm the effects of the impact angle on debris cloud characteristics.

CRediT authorship contribution statement

Samet Ceri: Writing – review & editing, Writing – original draft, Software, Methodology, Investigation, Data curation. **Zahra Sharif Khodaei:** Writing – review & editing, Supervision, Methodology, Conceptualization.

Declaration of competing interest

The authors declare the following financial interests/personal relationships which may be considered as potential competing interests: Samet CERI reports financial support was provided by Republic of Turkey Ministry of National Education. If there are other authors, they declare that they have no known competing financial interests or personal relationships that could have appeared to influence the work reported in this paper.

Data availability

Data will be made available on request.

Acknowledgments

The financial support provided for the first author from the Republic of Turkiye Ministry of National Education to undertake his PhD studies at Imperial College London, United Kingdom is gratefully acknowledged.

References

[1] Furumoto M, Hanada T. Adv Space Res 2018;62(3):533–41.
[2] Huang X, Yin C, Ru H, Zhao S, Deng Y, Guo Y, et al. Mater Des 2020;186:108323.
[3] Hyde J, Christiansen E, Bernhard R, Kerr J, Lear D. Eur Space Agency-Publ-Esa Sp 2001;473:191–6.
[4] Gongshun G, Baojun P, Wei Z, Yue H. Int J Impact Eng 2008;35(12):1541–6.
[5] Xue Z, Xie A, Zhu Y, Zhong Y, Wu Y, Zhou Y, et al. Int J Impact Eng 2021;154:103875.
[6] Hofmann DC, Bordeenithikasem P, Zhu Y, Liu Y, Conrad NJ, Davis BA, et al. Aerosp Sci Technol 2023;139:108372.
[7] Schonberg WP. Procedia Eng 2017;204:4–42.
[8] Liu M, Wang Q, Zhang Q, Long R, Su Z. Int J Impact Eng 2018;111:273–84.
[9] Liu M, Wang K, Lissenden CJ, Wang Q, Zhang Q, Long R, et al. Materials 2017;10(5):547.
[10] Verma PN, Dhote KD. Int J Impact Eng 2018;120:118–25.
[11] Zhang K, Chi R, Pang B. In: Shen G, Zhang J, Wu Z, editors. Advances in acoustic emission technology. Singapore: Springer Singapore; 2021, p. 475–86.
[12] He Q-G, Chen X, Chen J-F. Acta Astronaut 2020;175:99–117.
[13] Zhang Z, Qiang H, Gao W. Eng Struct 2011;33(1):255–64.
[14] Ba K, Gakwaya A. Comput Methods Appl Mech Engrg 2018.
[15] Liu M, Liu GR. Arch Comput Methods Eng 2010;17:25–76.
[16] Fulk DA, Quinn DW. J Comput Phys 1996;126(1):165–80.
[17] Oger G, Doring M, Alessandrini B, Ferrant P. J Comput Phys 2007;225(2):1472–92.
[18] Sun PN, Colagrossi A, Marrone S, Antuono M, Zhang AM. Comput Phys Comm 2018;224:63–80.
[19] Giannaros E, Kotzakolios A, Kostopoulos V, Campoli G. Int J Impact Eng 2019;123:56–69.
[20] Liu J, Wu C, Li J, Fang J, Su Y, Shao R. Int J Impact Eng 2019;125:143–62.
[21] Liu MB, Liu GR. Appl Numer Math 2006;56(1):19–36.
[22] Fourtakas G, Stansby PK, Rogers BD, Lind SJ. Comput Methods Appl Mech Engrg 2018;329:532–52.
[23] Das J, Holm H. J Ocean Eng Mar Energy 2018;4(2):153–69.
[24] Johnson GR, Stryk RA. Int J Impact Eng 2003;28(9):947–66.
[25] Fahrenthold EP, Horban BA. Int J Impact Eng 2001;26(1):169–78.
[26] Piekutowski AJ. Int J Impact Eng 1993;14(1–4):573–86.
[27] Zhang Y, An F, Liao S, Wu C, Liu J, Li Y. Aerospace 2022;9(1).
[28] Schonberg WP. Int J Impact Eng 2001;26(1):713–24.
[29] Schonberg WP, Ebrahim AR. Int J Impact Eng 1999;23(1, Part 2):823–34.
[30] Zhang Q, Chen Y, Huang F, Long R. Int J Impact Eng 2008;35(12):1884–91.

[31] Huang J, xia Ma Z, sheng Ren L, Li Y, xuan Zhou Z, Liu S. Int J Impact Eng 2013;56:32–9.
[32] Lamontagne CG, Manuelpillai GN, Taylor EA, Tennyson RC. Int J Impact Eng 2000;24(5):535.
[33] Piekutowski AJ. Int J Impact Eng 1997;20(6):639–50.
[34] Johnson GR, Stryk RA, Beissel SR, Holmquist TJ. Int J Impact Eng 2002;27(10):997–1013.
[35] Johnson GR, Beissel SR, Gerlach CA. Procedia Eng 2013;58:269–78.
[36] Yu S-x, Fan Q-b, Cheng X-w, Tan Y, Gao Y. J Mater Res Technol 2022;19:2115–25.
[37] Tadepalli SC, Erdemir A, Cavanagh PR. J Biomech 2011;44(12):2337–43.
[38] Burkhart TA, Andrews DM, Dunning CE. J Biomech 2013;46(9):1477–88.
[39] Erhart T. LS-DYNA forum. 2011.
[40] Hoque SE, Scheiblhofer S, Ucsnik S. 12th eur. LS-DYNA conf. 2019. Koblenz, Germany; 2019.
[41] Hallquist JO, et al. Livermore Softw Technol Corp 2007;970:299–800.
[42] Giambanco G, Fileccia Scimemi G, Spada A. Comput Mech 2012;50.
[43] Borrvall T. 7th eur. LS-DYNA conf.. Salzburg, Austria; 2009.
[44] Zhang C, Chen X, Yuan Y. Int J Impact Eng 2021;155(May):103908.
[45] Brundage AL. Procedia Eng 2013;58:461–70.
[46] Iyer KA, Poormon KL, Deacon RM, Mehoke DS, Swaminathan PK, Brown RC. Procedia Eng 2013;58:127–37.
[47] Myagkov NN, Stepanov VV. Phys A Stat Mech Appl 2014;410:120–30.
[48] Lye XY, Nakayama A, Nizamani Z. IOP Conf Ser: Earth Environ Sci 2021;945(1):012009.
[49] Mohseni-Mofidi S, Bierwisch C. Comput Part Mech 2020;8.
[50] Du Q, Liu F, Lei Q. Appl Sci 2023;13(15):8640.
[51] Ansys L. R12, southpoint. 2009.
[52] Wen K, Chen X-w, Lu Y-g. Def Technol 2021;17(6):1864–86.
[53] Piekutowski AJ. Int J Impact Eng 1995;17(4):627–38.